Liquid water quantification in the cathode side gas channels of a proton exchange membrane fuel cell through two-phase flow visualization

CrossMark

Rupak Banerjee, Satish G. Kandlikar*

Mechanical Engineering and Microsystems Engineering, Rochester Institute of Technology, Rochester, NY 14623, USA

HIGHLIGHTS

- Liquid water in the cathode side channels of PEM fuel cell is quantified.
- Algorithm developed in MATLAB® to quantify liquid water in two-phase flow.
- Dominant flow patterns detected and quantified for each condition.
- The variation of liquid water in individual channels is compared.
- Correlation developed to predict ACR at different operating conditions.

ARTICLE INFO

ABSTRACT

Water management is crucial to the performance of PEM fuel cells. Water is generated as part of the electrochemical reaction, and is removed through the reactant channels. This results in two-phase flow in the reactant channels. Increased understanding of the behavior of the liquid water in the channels allows us to devise better strategies for managing the water content inside the fuel cell. Most previous work has been focused on qualitative information regarding flow pattern maps. The current work presents new algorithms developed in MATLAB® to quantify the liquid water and to identify the flow patterns in the cathode side reactant channels. Parallel channels with dimensions matching those of commercial stacks have been used in this study. The liquid water present in the reactant channels is quantified for different temperature, inlet RH and current density conditions, and the results are presented in terms of area coverage ratio. The dominant flow patterns for the different conditions have been mapped, and trends interpreted on the basis of air flow velocities and saturation conditions within the channels.

1. Introduction

1.1. Overview

PEM fuel cells generate electrical energy from the electrochemical reaction of hydrogen and oxygen. Water is a by-product of the reaction. Water management remains a crucial limiting factor in the performance enhancement of proton exchange membrane fuel cells (PEMFCs) [1–8]. Understanding the two-phase flow of water and reactants in the flow field channels (of PEMFCs) has received significant attention in the past few years [1,5,7,9–14]. Most of the work has focused on the two-phase pressure drop in the reactant channels as the method for defining effectiveness of water management within the cell [5,9,10]. It has been identified as an important diagnostic tool for PEMFC performance [15].

The liquid water present in the gas channels affects the performance in two ways. Increased flow resistance decreases the reactant flow and causes localized starvation down the channel from the liquid water features. It also reduces the area available for diffusive mass transport into the GDL and increases the diffusion resistance for the reactants. Therefore it is important to quantify the liquid water present in the gas channels.

Transparent fuel cells have been used by different researchers to understand the behavior of liquid water in the reactant channels of

* Corresponding author. Tel.: +1 585 475 6728; fax: +1 585 475 7710.
 E-mail address: sgkeme@rit.edu (S.G. Kandlikar).

an operating PEMFC [16–21]. However, most studies have focused on the qualitative evaluation of the liquid water features, such as identification of flow patterns, without providing quantitative information.

1.2. Literature review

The product water from the electrochemical reaction emerges into the channels, and is then removed from the cell. Water is removed in the form of vapor carried in the gas stream, and also as liquid water in the reactant channels. Various visualization techniques have been used to investigate the liquid water present in the reactant channels [15,16,18].

Neutron imaging has been used successfully while studying the presence of water in PEMFCs [19,22–25]. The water has high interaction with the neutrons, while PEMFC materials have low interactions. Kramer et al. [24] used neutron imaging to investigate liquid water in the flow fields, achieving a spatial resolution of 115 μm/pixel and a temporal resolution of 2 frames per second (fps). Access to neutron sources remains limited and expensive. Additionally, the temporal resolution is too low to observe changes in water flow patterns in the flow fields. Rapidly moving water features may travel at up to 1 m s^{-1} which would display as a thin film, leading to incorrect conclusions [19]. Therefore, neutron imaging, although well-suited to measuring saturation of the GDL or the MEA, would not be as accurate for quantifying liquid water in the flow fields.

X-rays have also been used for imaging of fuel cells [26–28]. However, as metals attenuate the high energy waves, modifications must be made to enable the X-rays to penetrate. Manke et al. [26] utilized high spatial resolution to study formation of liquid water inside individual pores of GDL. Although high temporal resolution can be obtained, it comes at the cost of spatial resolution. Thus, high

temporal and spatial resolutions cannot be obtained simultaneously. Lee et al. [28] also used X-rays to visualize the temporal change in liquid water quantity within the cell. The study observed the cell from the in-plane direction: the thickness of the liquid water features was their focus.

Dunbar and Masel [29] used magnetic resonance imaging to study water distribution. They reported a 3D water concentration profile for the operational fuel cell. They successfully demonstrated that the majority of the water content was present on the cathode side.

Optical imaging systems have been around for centuries. They are easy to operate, accessible and cost effective. The maximum resolution is limited by the Rayleigh criterion at about 200 nm. However, the operating region for water management research in the flow fields is only limited by the quality of camera being used. Typical PEMFCs do not use optically transparent materials, and therefore require modifications and inclusion of optically transparent windows. One of the concerns with introducing this modification is the effect it has on the parameter being studied: in this case, the two-phase flow in reactant channels [30].

Optical imaging has been used to study water management in PEMFCs using in situ studies [17,19,20,31–36] as well as ex-situ investigations [37–41]. Various imaging techniques have been used to obtain qualitative data pertinent to liquid water within the reactant channels. Hussaini and Wang [33] quantified liquid water in the cathode channels for the first time in 2009. However, the focus of their work remained spatial quantification: they recorded static images after 30 min of operation, assuming that steady state condition had been achieved. Nirunsin and Khunatorn [34] used optical imaging to quantify the water in a single serpentine channel PEMFC. They investigated the change in liquid water coverage of the channel area with temperature and stoichiometry.
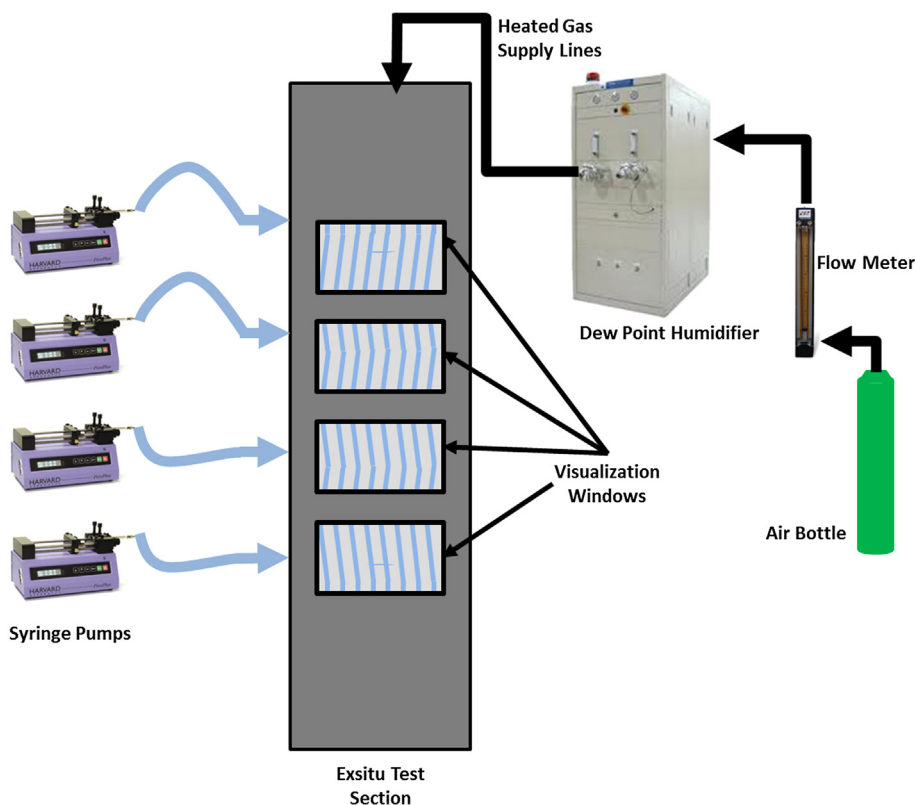

Fig. 1. Schematic of the ex-situ test setup used in this work.

Sergi and Kandlikar [31] developed a dual visualization setup to simultaneously observe both the anode and cathode gas channels to understand the two-phase flow. They reported the development of an image processing algorithm to quantify the liquid water in the channels. An additional algorithm was developed to investigate the transition between flow patterns in the channels. A new method had been established for using optical imaging with image processing to observe and quantify the two-phase flow in PEMFC gas channels.

Although several attempts have been made to quantify the liquid water in the PEMFC gas channels, a systematic study showing the effect of operating conditions on the liquid water presence in the cathode reactant channels is still lacking. This work attempts to generate quantitative data in the form of area coverage ratio (ACR) and to establish trends for two-phase flow in PEMFC gas channels. An ex-situ experimental setup is used to emulate the cathode side gas channels of the PEMFC. A modified form of the algorithms used by Sergi and Kandlikar [31] was utilized in this work to obtain water quantification data at different flow and temperature conditions.

Optical imaging system is selected for this work because of the high spatial and temporal resolution and the ease of operation. Previous works have shown the feasibility of using optical imaging systems to observe and investigate the two-phase flow in PEMFC reactant channels. However, a common problem encountered in using an optically visual cell is mass transport driven cell performance loss at low current densities. Current densities above 1.0 A cm^{-2} have not been tested in the in situ visualization studies due to this problem. However, state of the art fuel cells are able to achieve much higher current densities and therefore an ex-situ study is necessary to complement and provide the quantification data for liquid water presence in the channels. This study aims to provide the quantification of liquid water in the PEMFC reactant channels for different operational conditions simulated in an ex-situ setup.
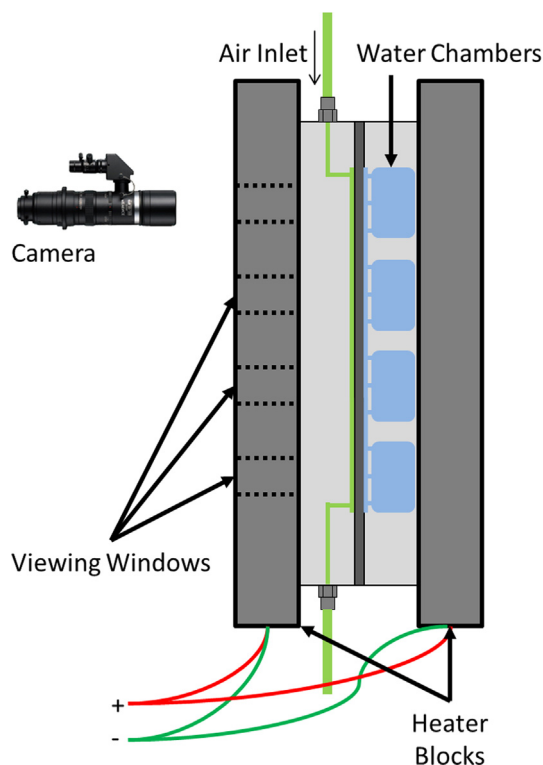
Table 1
Flow rates associated with equivalent current densities reported in this work.

Eq. current density (A cm^{-2})	Stoichiometric ratio	Air flow rate (ml min^{-1})	Rate of water generation (µl min^{-1})
0.1	3	101	2.6
0.4	2	268	10.3
0.7	2	470	18.1
1.0	2	671	25.8
1.3	2	872	33.6
1.5	2	1006	38.7
2.0	2	1342	51.7
2.5	2	1677	64.6
3.0	2	2013	77.5

The liquid water coverage of the GDL surface reduces the available surface area for gas transport from the channels to the catalyst layer. Quantifying this effect, in terms of the ACR as a function of operating parameters is the major goal of this work. The results discussed in this work can directly be incorporated into a modeling effort, and used as a reduction in surface area for gas transport and a flow resistance in the reactant channel.

2. Experimental setup

2.1. Ex-situ setup

An ex-situ setup has been used in this work. The setup is modified from a setup used in previous studies [37,38]. Being an ex-situ setup, the electrochemical reaction is not taken into consideration. A schematic of the test setup is shown in Fig. 1 and a cross sectional view is given in Fig. 2.

Ultra zero grade air is supplied from pressurized bottles. The flow is metered, based on the equivalent current density being tested. The volumetric flow rate of air required to sustain an equivalent current density with appropriate stoichiometry is calculated at room temperature and atmospheric pressure using Faradays' law. Table 1 shows the corresponding air flow rate and rate of water generation calculated for each current density. The air is then heated and humidified to the appropriate level using an Arbin dew point humidifier (DPHS-D50), which controls the dew point and gas temperatures. The gases are delivered to the test section via heated gas lines to ensure no loss in temperature and to avoid condensation. The test section is heated to ensure an isothermal setup. Two sets of electrical heaters are used to heat the front and back plates. Twelve thermocouples located throughout the test section and the heater plates monitor the system temperature to ensure isothermal condition.

The test section shown in Fig. 2 consists of heater blocks, gas channel, water channels, and the GDL. The GDL is compressed between the air channel and the water channels. The dimensions for the air channels represent the reactant channels on the cathode side. The water channels distribute water evenly over the MPL side of the porous media, mimicking water generation at the catalyst layer. The water channels are supplied through a buffer of water chambers which damp out any pressure fluctuations from the syringe pumps. The water chambers are also heated to ensure the water is injected into the system at the isothermal condition. Four

Fig. 2. Cross-sectional schematic of the ex-situ test section.

Table 2
Matrix of experimental test conditions used in this work.

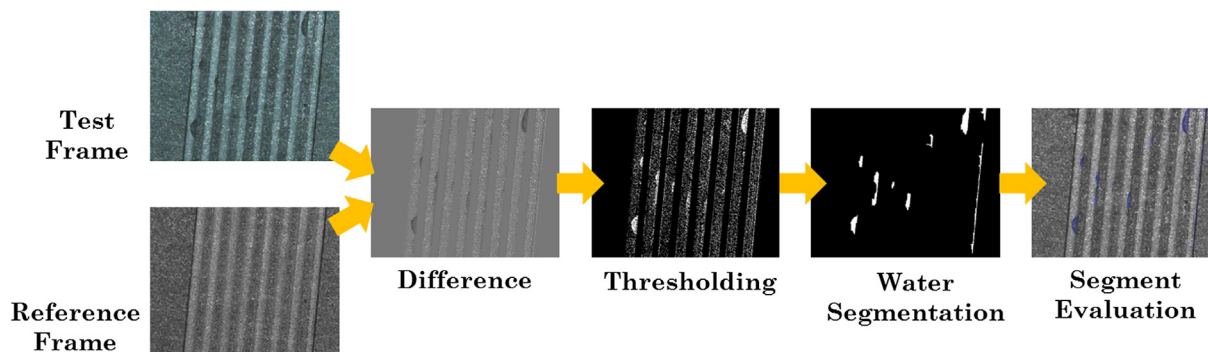| Tested parameters	Values
Eq. current density	0.1–3.0 A cm^{-2}
Temperature	23, 40, and 60 °C
Relative humidity of inlet gases	0, 50, and 100% RH
Stoic	2 (3 for 0.1 A cm^{-2})

Fig. 3. Graphical representation of the algorithm used for ACR (Area Coverage Ratio).

separate chambers promote an even distribution of water along the length of the channels.

The gas channels are 183 mm long, and are 0.7 mm wide × 0.4 mm deep in cross-section. The gas channels are separated by 0.5 mm wide land regions. The channels incorporate a 5° switchback design to avoid mechanical shearing of the GDL associated with straight channels. The equivalent area under consideration (18.4 cm^2) houses 8 channels in the cathode side reactant channel configuration. The channel dimensions are based on the Department of Energy targets set for automotive applications as described by Owejan et al. [11]. The gas channels were manufactured in Lexan® for optical clarity. Also the contact angle of Lexan® matches graphite very closely, which is commonly used in fuel cell bipolar plates. The resulting test section simulates the water generation on the cathode side and the two-phase flow of air and water in the cathode side reactant channels.

The gas channels are supplied through an inlet manifold and the two-phase fluid is collected at the exit manifold. The manifolds also serve the purpose of two-phase pressure measurement using Honeywell differential pressure sensor with a range of 0–35 kPa and an accuracy of 0.25% of the full range, i.e. a maximum uncertainty of 88 Pa in the reading.

The GDL used in this work is MRC U-105 with 5 wt.% PTFE, provided by General Motors (GM) and coated by GM in-house with an MPL on one side. The GDL has an uncompressed thickness of 235 μm and has a PTFE gasket of 178 μm thickness surrounding it on all four sides. PTFE gasket is used to act as a 'hard stop' ensuring a known thickness after the initial compression.

2.2. Test matrix conditions

Fuel cell operating conditions in automotive applications change depending on environmental conditions, operational time and performance requirement. Gas temperatures being supplied to the cell start at ambient temperatures, though they are supplied at

higher temperatures later. The cell temperatures reflect the ambient temperatures at start-up. As the time of operation increases, the cell reaches higher temperatures due to the heat generated (which can be up to 100 kW for a commercial stack). Cell temperatures are maintained using a cooling system. Different cooling techniques used for regulating temperatures within the fuel cell are discussed by Zhang and Kandlikar [42]. The cell temperatures are often maintained between 60 and 80 °C to obtain high cell efficiency and for efficient water removal [43–46]. The effect of different temperatures on the liquid water coverage in the reactant channels is investigated in the current work.

At 80 °C, the saturation pressure increases significantly as compared to 20 °C (2.62 kPa at 22 °C vs. 51 kPa at 80 °C [47]) and the mass of water required to saturate the air stream is much higher. If dry gases are introduced at the inlet of the fuel cell, the water being generated at the cathode catalyst layer is insufficient to keep the membrane hydrated. Therefore inlet gases are humidified in order to maintain the hydration of the membrane. The effect of different levels of humidification of the inlet gases on the liquid water coverage in the reactant channels has been studied.

A typical polarization curve and a power generation curve show that peak power density is obtained at higher current densities. Increased current densities require higher air flow rates and result in higher air flow velocities. They also result in higher water generation rates, and introduce more water that needs to be removed from the cell. Table 1 maps the different air flow rates required for the different current densities and the rates of water generation. The stoichiometry used to calculate the air flow rates is 2 for all conditions, but is changed to 3 for the current density of 0.1 A cm^{-2}, which is associated with very low flow rates and therefore cannot be sustained under in situ conditions. Higher flow rates are required to minimize the losses and keep the reaction going. The resulting set of test conditions is shown in Table 2.

2.3. Experimental protocol

The current work focusses on the liquid water coverage in the gas channels. Videos are recorded at 30 frames per second for 360 s
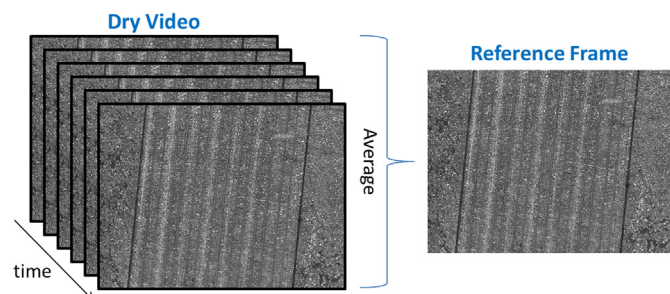

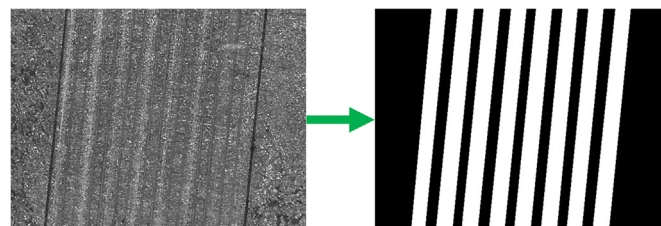**Fig. 4.** Reference frame obtained by averaging frames from a dry video.

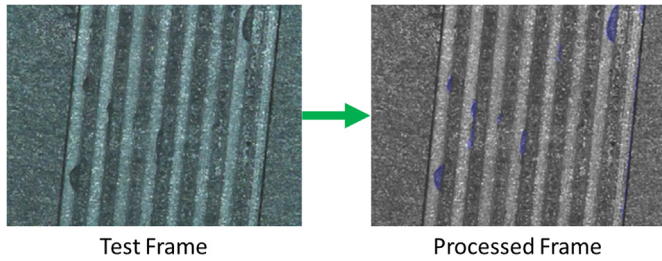**Fig. 5.** Creating of a mask file from reference frame.

Fig. 6. Processed frame is used for visual inspection of processing quality.

at each of the four windows. A shutter speed of 1/250 s is employed to reduce blurring of images in case of faster moving water features. The total time required for recording at each window is 6 min with equal time required to save the file, requiring 48 min to capture videos for all four windows.

Linear motorized stages manufactured by Velmex Inc. are used to accurately and repeatedly position the camera to exactly the same location on each window. This allows test videos to be recorded at the same locations for each condition. In addition to the test videos, dry videos are recorded before introducing any water to the test sections. These dry videos are used to provide reference frames for detecting water in the test videos.

Pressure drop is recorded using the differential pressure sensors described earlier. Single phase pressure drop is recorded for each of the air flow rates corresponding to the equivalent current densities shown in Table 1. During each test, the two-phase pressure drop is recorded for a total of 60 min to average the fluctuations in the two-phase pressure measurements. The commonly observed flow patterns of slug flow, film flow, and mist flow result in their characteristic pressure drop signatures [10]. The same pressure drop signatures were observed during the current tests. Averaging the pressure-drop data over 60 min avoided biasing from the pressure spikes associated with two-phase flow, especially in the slug flow regime.

The two-phase pressure drop measurement is used in obtaining the two-phase gas multipliers as defined by Ref. [37] and shown in Equation (1). The two-phase gas multiplier ($\phi_{\mathbf{g}}^2$) is the ratio of the two-phase pressure drop ($\Delta \mathbf{P}_{2\phi}$) to the single-phase pressure drop ($\Delta \mathbf{P}_g$). This provides an easy and convenient method of reporting on the impact the liquid phase has on the pressure drop in the system.

$$\phi_{\mathbf{g}}^2 = \frac{\Delta \mathbf{P}_{2\phi}}{\Delta \mathbf{P}_g} \qquad (1)$$

3. Methodology of image analysis

The videos recorded as part of the testing protocol are used to quantify the water in the gas flow channels. Each test video is treated as a sequence of images. An algorithm developed in MATLAB® is used to extract relevant information about liquid water present in the channels. The water is quantified as the Area Coverage Ratio (ACR) and is defined as the fraction of interfacial area covered by liquid water present in the flow channels. Another algorithm is used to identify the water features present in the channels and classify them in terms of slug flow or film flow. Details of both the algorithms are mentioned in the following sections.

3.1. Area coverage ratio

The algorithm developed for obtaining the Area Coverage Ratio (ACR) processes each video on a frame by frame basis through a MATLAB® program. A graphic representation of the algorithm is shown in Fig. 3. The first phase of the algorithm is responsible for image segmentation, which refers to the division of an image into different regions, based on specific properties [48]. In this case, image segmentation is used to identify the regions of liquid water within each image frame. A reference frame (R_{ij}) was obtained by averaging frames from a dry video (discussed in Section 2.3) as shown in Fig. 4. The test video was compiled into an output video for optical evaluation of the accuracy of processing. The reference frame is subtracted from test frame (W_{ij}) to obtain a difference image frame (D_{ij}) as shown in Equation (2).

$$D_{ij} = W_{ij} - R_{ij} \qquad (2)$$

Absorption of the incident light provides significant contrast between GDL regions and water regions. The liquid water shows up much darker in the test frames, compared to the surrounding. Thus, a single sided threshold is adequate to isolate the regions of liquid water in the channels (Equation (3)), producing the threshold image (G_{ij}). The difference image is evaluated for pixel intensities, with pixels below a threshold value representing water regions. The pixels identified as water regions are allocated the value of 1, while the remaining regions are 0. Thus, a binary image of the water locations is obtained.

$$G_{ij} = \begin{cases} 1 & D_{ij} > \text{Threshold} \\ 0 & D_{ij} < \text{Threshold} \end{cases} \qquad (3)$$
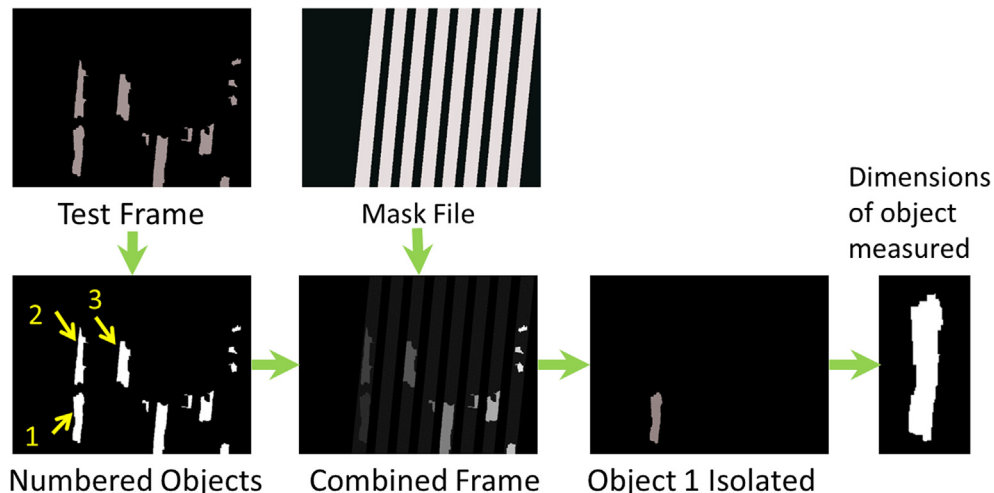

Fig. 7. Graphical representation of the algorithm used to identify the flow regimes (Flow Identification Algorithm).
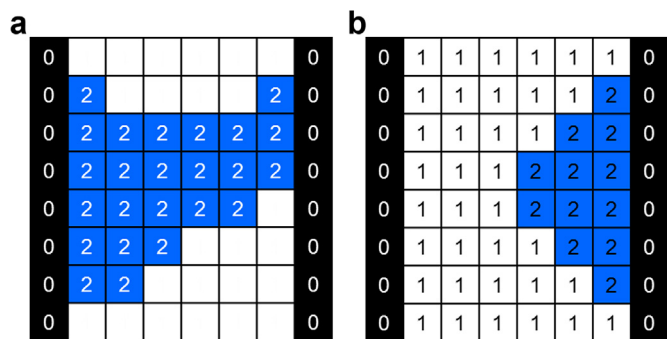
Fig. 8. If the channel is completely bridged by water, it is classified as slug flow (fig a). If the channel is not bridged completely, it is classified as film flow (fig b).

At this step, the water regions are isolated. However, both the reference image and the test image contain noise which percolates through the above stages to the threshold image, and morphological image processing steps need to be applied to refine the water segmentation. A binary mask file is created from the reference frame (Fig. 5) such that the channel regions are foreground (1s) and land regions are background (0s). The threshold image (G_{ij}) is multiplied by the mask file to restrict future processing steps to the channel regions only.

Morphological processing has been shown to be important for accurate detection of water by Sergi and Kandlikar [31]. The first step involves checking for connected clusters of pixels in the foreground. One hundred pixels were chosen as a representative of small water features. For checking for irregular structures such as water features, 8-connectivity is used. Water features larger than 100 pixels remain, while smaller features are considered as 'noise' and are discarded. Just as 'noise' can be detected as water pixels, it can result in some water pixels to be below the threshold, and therefore be neglected. However, holes can be filled in the binary image [48] by checking for connection with the background pixels. If a region of background pixels exists completely surrounded by foreground pixels, it is converted to foreground. This is implemented using a predefined MATLAB® function.

A closing operation is used as the final operation in the morphological processing phase. The closing operation is a dilation step followed by an erosion step. It is used to smooth the contours of the foreground water features. A disc of 5 pixel radius is used as the structuring element for best results. This concludes the morphological processing, and provides the final binary image identifying the liquid water features.

This foreground of the binary image is converted to a faint blue and then added to the original test frame. The frames are finally sequenced to form the final video output. The output video highlights the water regions in the faint blue so that they can be visually inspected for the quality of the processing (Fig. 6).

The channel pixels in the mask (Fig. 5) define the interfacial area between the GDL and the gas channels available for reactant transport. The final processed frame in the ACR algorithm is a binary image with the foreground pixels representing liquid water. ACR is obtained at each frame by taking the ratio of the water pixels in the processed frame to the channel pixels of the mask file. The ratio is calculated for every frame in the video. The mean ACR is reported for each window. The final ACR value to be reported for every condition is the average of the ACR values reported at each window.

$$\text{Area Coverage Ratio} = \frac{\text{Interfacial area blocked by liquid water}}{\text{Total interfacial area of GDL}}$$
(4)

Thus the final reported value of ACR is spatially averaged over the length of the channels and is temporally averaged over the entire recording time of 48 min.

3.2. Flow identification algorithm

A second algorithm has been developed to identify the different two-phase flow regimes dominant in the gas channel for PEMFC conditions. It has been shown in previous work that slug flow, film flow, and mist flow are the three most commonly observed flow regimes reported in two-phase flow studies pertaining to PEMFC gas channels [10,37]. The algorithm detects slug flow and film flow but not mist flow. Mist flow is not captured in the images. Fig. 7 shows the graphical representation of the algorithm.

Each test video is processed on a frame by frame basis. The first step involves numbering each water feature in an ascending order, from left to right. This frame is then added to a mask file (discussed in Fig. 5). The binary mask file universally adds one to the numbered objects frame. The channels are now numbered as 1s, the land regions are numbered 0s and the water features are numbered from 2 onwards to the number of objects present.

Each object is then selected and evaluated to distinguish between a slug feature and a film feature in the channel. The two sides of the water features (object) are evaluated for pixel values. If both sides are zeros (representing land region), the object bridges the entire channel and therefore is considered as a slug, shown in Fig. 8a. If one of the sides is a pixel of value 1, it represents the object with one boundary within the channel. Thus the water feature does not bridge the entire channel and is a film on the channel wall, shown in Fig. 8b.
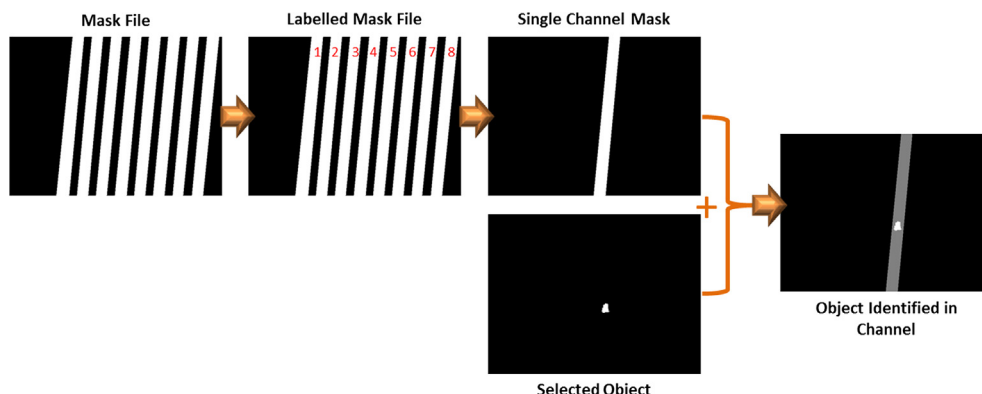

Fig. 9. Graphical representation of the algorithm used to find variation in channel-to-channel liquid water area coverage ratio.
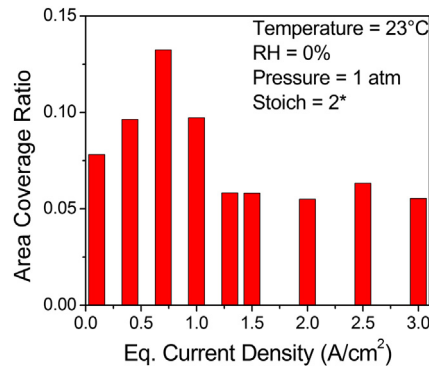
Fig. 10. Area coverage ratio for 23 °C temperature with air inlet at 0% RH.

The row vector of the topmost pixel and that of the lowest pixel of an object are also evaluated to obtain the length of the water feature. If the object is determined to be a film, the film width is found by the same technique as the length of the object was. This extra information is stored in a file, but not utilized in the current work.

3.3. Channel to channel variation of liquid water

When a single inlet header is used to supply a gas to multiple channels, such as in our current setup, the channels are subjected to flow maldistribution. This maldistribution in PEMFC reactant channels was documented and quantified by Kandlikar et al. [37,49]. The effect of flow maldistribution on the liquid water coverage in the gas channels has not been investigated. The information in the test videos should enable us to investigate the variation in ACR in the different channels.

Fig. 9 shows a graphical representation of the algorithm used to detect the variation in liquid water presence in the different channels. The water segmented file generated in the first algorithm (area coverage ratio algorithm) is used to compare the water in the different channels. The mask file is imported and labeled from left to right in an ascending order. The frame with the water object is added to the mask file. Each single channel mask is cycled through, to check for values greater than 1. Once it is established into which channel the object is located, the size of the water object is assigned to the channel. Each object (in all the frames) is processed through the same process, to classify all liquid water in terms of the channel in which it is located. The process is then repeated for all frames and all videos of the tested condition.

4. Results and discussion

4.1. Area coverage ratio results

Results from the Area Coverage Ratio (ACR) processing are discussed in this section. Figs. 10 and 11 show the ACR for different temperature and relative humidity conditions. Higher current densities along the x-axis correspond to higher air flow rates, as shown in Table 1. In Fig. 10 it is seen that the ACR increases with increased equivalent current densities until 0.7 A cm^{-2}, and starts to decrease thereafter at higher current densities. A similar trend was also observed during in situ studies by Sergi and Kandlikar [31], although the peak ACR was observed at a lower current density. The ACR plot shows two trends. The ACR increases with increased eq. current densities until a current density of 0.7 A cm^{-2} is reached. This may be attributed to the fact that greater quantity of water is being generated, and consequently more liquid water is being introduced into the reactant channels. The same data points correspond to the high two-phase multipliers in the adjoining plot. The second trend observed is that of decreasing ACR at the higher current densities. This is attributed to higher air velocities, resulting in shorter residence times for the liquid water features. The liquid water is being removed at a faster rate; when averaged over time, the overall ACR begins to decrease and then stabilize as both the effects reach equilibrium. This is also reflected in the pressure-drop multipliers which stabilize at a fairly low value of 1.2 at the higher current density values.

Fig. 11 shows the ACR obtained at 40 °C with 0, 50 and 100% inlet RH respectively. For each of the conditions, we observe that the ACR decreases with increased equivalent current density. Comparing the three, we note that with 100% inlet RH, the quantity of liquid water is
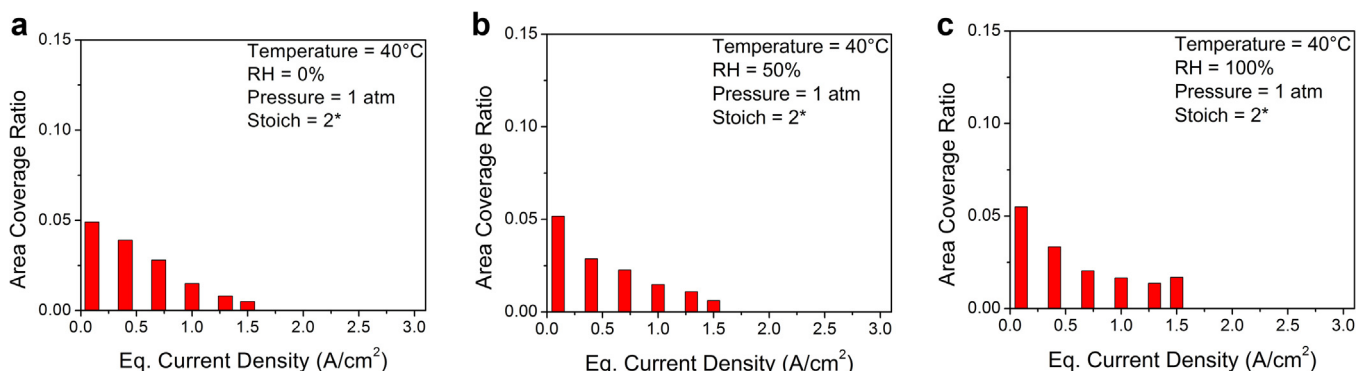

Fig. 11. Area coverage ratio for 40 °C temperature with air inlet at 0, 50 and 100% RH at the inlet.
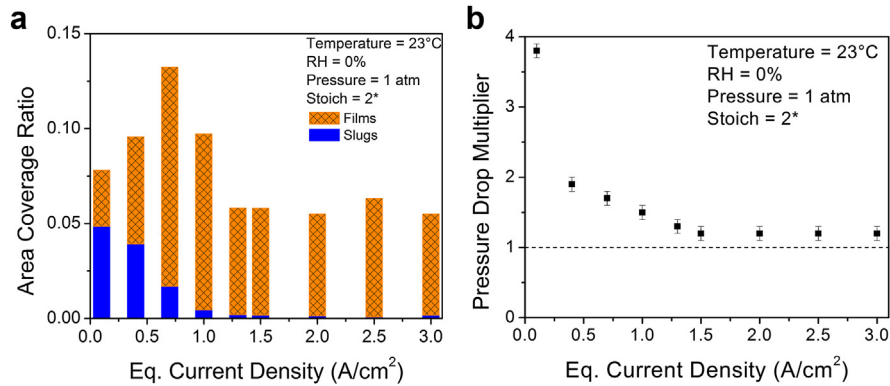
Fig. 12. Flow regime identification results and two-phase pressure drop multiplier for 23 °C temperature with air inlet at 0% RH.

higher than equivalent cases with inlet gases being at 0 or 50% RH as expected. ACR was also calculated for the three relative humidity conditions at 60 °C (0, 50 and 100% inlet RH). The ACR quantified in each of these conditions was on the order of 0.001, therefore negligible in comparison to the liquid water at 23 and 40 °C.

When temperature increases from 23 °C to 40 °C and then onto 60 °C, there is a noticeable change in the trends. Instead of the dual trend observed at ambient temperatures, only a single dominant trend is observed at 40 °C. The increased temperature changes the condition in two ways. One: the saturation pressure increases such that, at the lower inlet RH values, most of the water is taken up by the air stream in vapor form, thereby leaving less liquid water in the channels. Second: the increased temperature and RH condition increases the total mass of gases flowing through the channels. This increases the air velocities, reducing the residence times of the liquid water features.

4.2. Flow identification results

Fig. 12 shows the dominant flow regimes for increasing current densities at ambient room temperature of 23 °C and a dry inlet condition. We can observe that the higher current densities are dominated by film flow regime, whereas significant slug flow is present at the lower current densities. The occurrence of slug flow decreases with increasing current densities and there is no significant slug flow after 1.0 A cm^{-2}. From the adjoining figure, we also observe that the two-phase multiplier decreases with increased eq. current densities. At the lower eq. current densities, slug flow is dominant resulting in the higher two-phase multiplier. As the current density increases, air flow velocities increase, resulting in increased contribution of film flow. The two-

phase multiplier decreases with increased contribution of film flow. Beyond an equivalent current density of 1.0 A cm^{-2}, we note that the ACR is primarily in the film flow regime, and the two-phase multiplier decreases to an asymptotic value of 1.2. We note that the two-phase multiplier reflects the findings of the ACR.

Fig. 13 shows the flow regimes present at different current densities at a temperature of 40 °C. For dry inlet condition, only the lowest current density of 0.1 A cm^{-2} has some slug flow, and the film flow is dominant. This minimal slug flow is not present for the condition of 50 and 100% inlet RH. The higher current densities are dominated by the film flow only. Therefore, at the higher temperatures, only film flow is present in the reactant channels. The increased temperature leads to higher saturation pressures, and therefore less liquid water in the channels. The ratio of water to air reduces thereby promoting film flow. Additionally, the increased air velocities (due to the increase in temperature and RH) lead to film flow being the dominant flow regime at these conditions.

4.3. Results for channel to channel variation in ACR

It was previously established that the flow rates of individual channels vary in the case of parallel channel configuration. This leads to a variation in pressure drop in the individual channels [49]. An equivalent study in the variation of liquid water presence in the reactant channels of the PEMFC is conducted. Fig. 14 shows the ratios of liquid water detected in the different channels. The ex-situ setup has 8 channels showing the variation in the liquid coverage ratios. The figure has 6 plots for 6 different flow rate conditions mapped to equivalent current densities of 0.1–1.5 A cm^{-2}. From
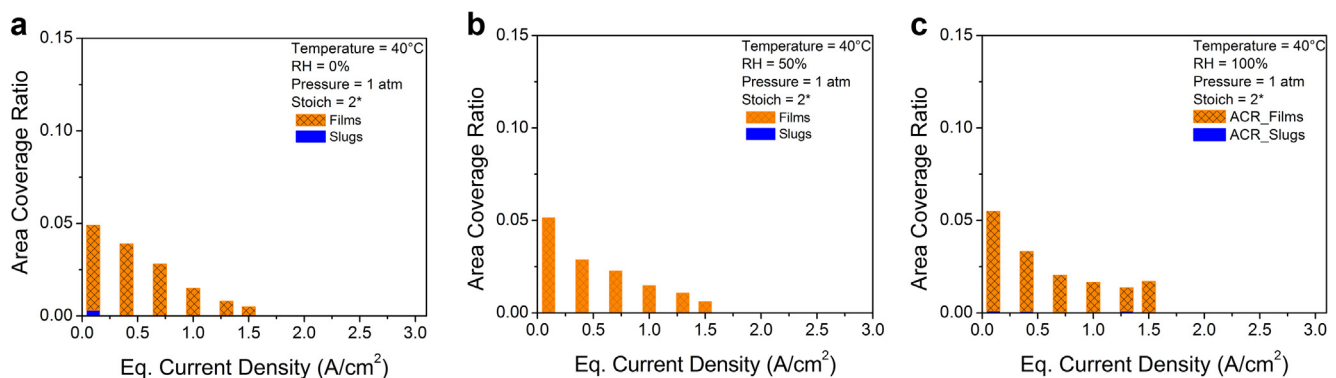

Fig. 13. Flow regime identification results for 40 °C temperature with air inlet at 0, 50 and 100% RH.
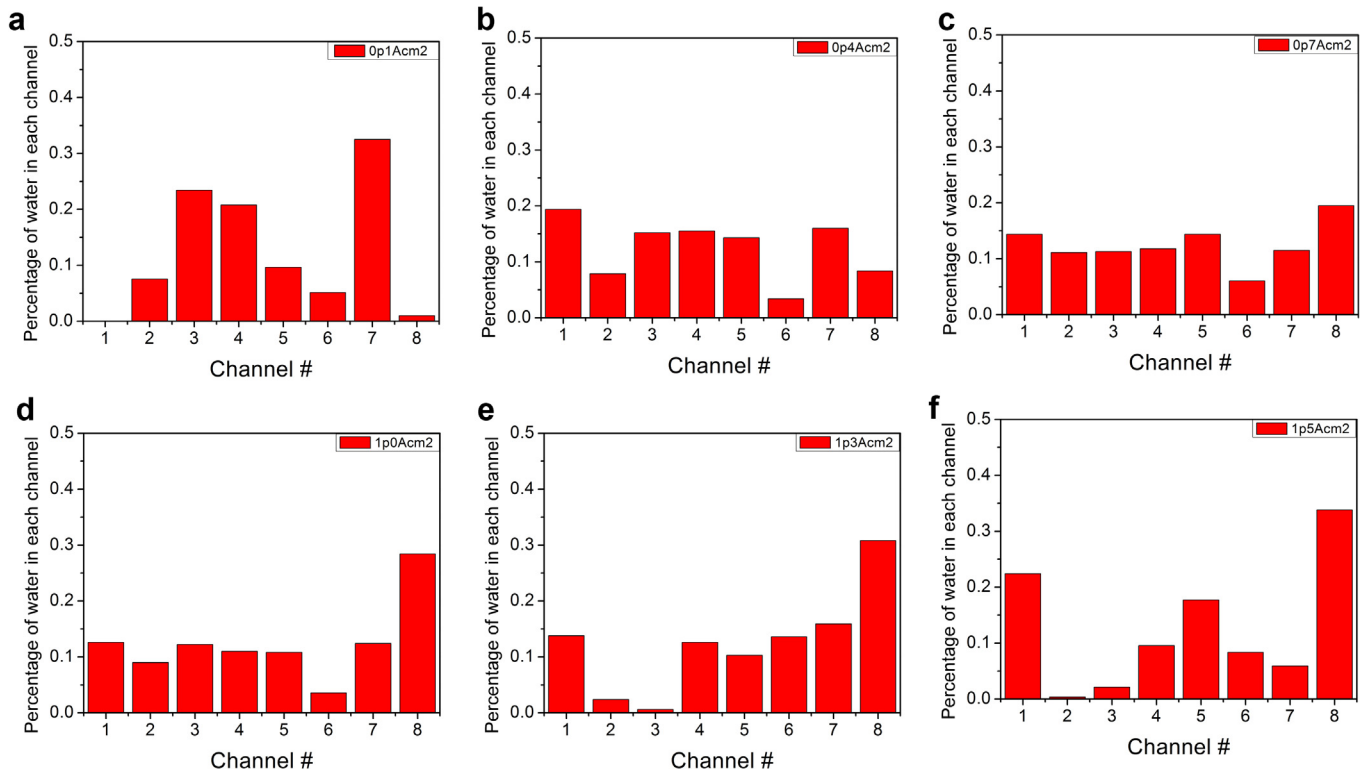
Fig. 14. Channel-to-channel variation in the liquid water area coverage for 6 different current densities, at ambient temperatures.

these plots, we note that all of the channels have water being detected at different levels. There is no particular trend observed in the channel-to-channel variation of liquid water coverage of the reactant channels.

The lack of a definite trend indicates that the water being detected is based on the different channels to which the GDL is feeding water. It has been established by Lu et al. [50] that GDL with MPL have intermittent drainage characteristics which result in established flow paths through the GDL. Therefore water enters the same channel repeatedly. However, no particular characteristics can be seen in the channels. This indicates that there is no evidence of any of the channels having a biased presence or absence of liquid water.

4.4. Comparison to neutron radiography results on DOE project website

In situ testing of identical GDL and cathode reactant channels has been done at identical operating conditions, and neutron radiographs have been obtained. This data is reported in public domain on the website being maintained by General Motors (www.pemfcdata.org). Figs. 15–17 show the neutron radiographs for different conditions at 40 °C. Liquid water in the channels shows up as red marks due to the thickness of water. The blue and green regions represent water present in the GDL and the membrane. From these figures, it is seen that more liquid water is present at the lower current densities, which is directly related to lower
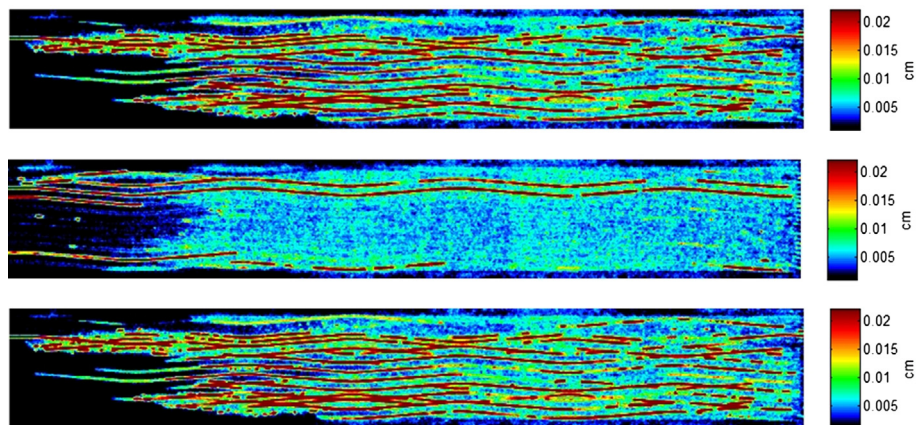

Fig. 15. Neutron radiography data image for 40 °C temperature with cathode inlet at 0% RH for current densities of 0.1, 0.4 and 1.5 A cm^{-2} respectively from top to bottom (www.pemfcdata.org).
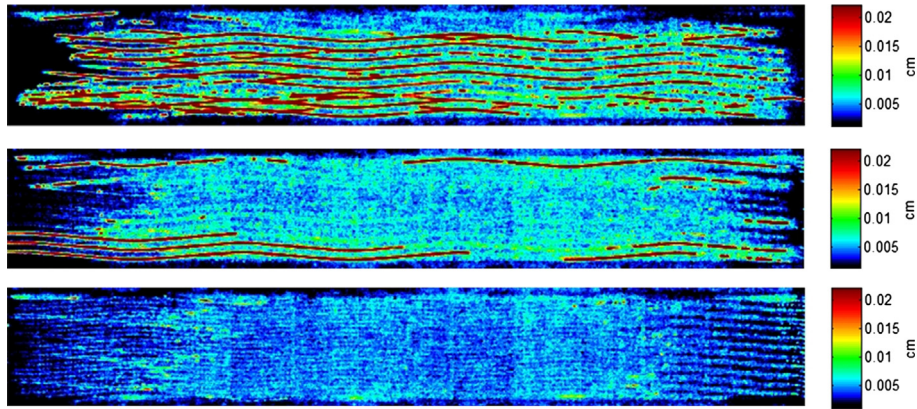
Fig. 16. Neutron radiography data image for 40 °C temperature with cathode inlet at 50% RH for current densities of 0.1, 0.4 and 1.5 A cm^{-2} respectively from top to bottom (www. pemfcdata.org).
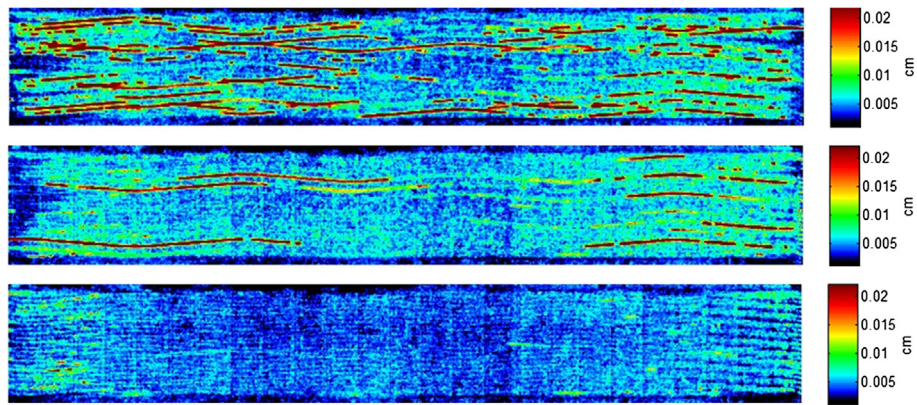

Fig. 17. Neutron radiography data image for 40 °C temperature with cathode inlet at 95% RH for current density of 0.1, 0.4 and 1.5 A cm^{-2} respectively from top to bottom (www. pemfcdata.org).

superficial gas velocities. At the higher inlet RH conditions, there is a greater mass of gases flowing into the reactant channels, and therefore the gaseous superficial velocities are higher. These result in more of the liquid water being removed, with the dominant flow regime being film flow. The in situ tests establish that the results seen in the current work under ex-situ conditions hold true during in situ operation of PEMFC.
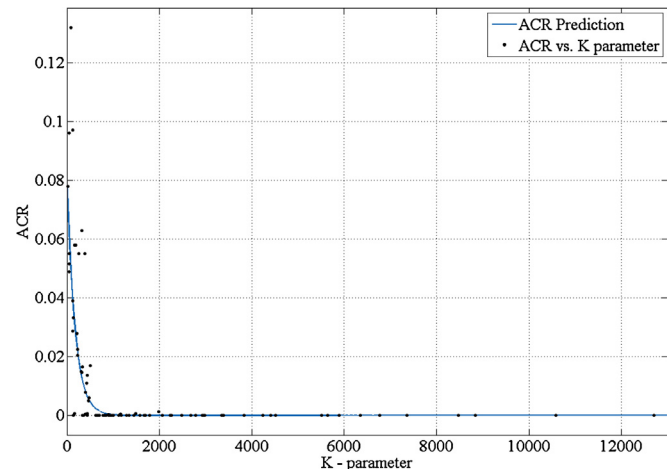

Fig. 18. Comparison of predicted and experimental ACR for the entire data set with 90 unique data points.

4.5. ACR correlation

The results discussed in Section 4.1 and 4.2 show us that the liquid water in the cathode reactant channel, quantified as the ACR is affected by the current density and the temperature, while the relative humidity does not seem to have a profound effect on the ACR. Increasing current density also increases the gas superficial velocity in the channels, which in turn dictate the ACR and the flow transition from slug flow to film flow [10].

A correlation is proposed based on the experimental data obtained in this study. As the two major factors playing a key role in predicting ACR would be the gas superficial velocity and temperature, a parameter K is defined to take the two parameters into consideration. The change in temperature of cell affects the saturation pressure of water in the gases and therefore dictates how much water can be removed in the vapor phase. Thus, the effect of pressure is considered using the saturation pressure. Equation (5) below defines K as the product of the gas superficial velocity, u (m s^{-1}) and the saturation pressure, P_{sat} (kPa).

$$K = u*P_{\text{sat}} \tag{5}$$

P_{sat} increases exponentially with regard to temperature. The superficial gas velocity increases with increased temperature and relative humidity conditions. The following correlation is proposed to predict the Area Coverage Ratio for given operating conditions.

$$ACR = a*\exp(b*K) \tag{6}$$

where, $a = 0.07876$ and $b = -0.005655$, constants based on the operating conditions.

Fig. 18 shows the comparison of the predicted and experimental ACR plotted against the parameter K, defined in Equation (5). The difference between the prediction and experimental ACR is found to be less than 20% over the entire range. This difference takes into consideration 90 unique data points tested as part of this investigation.

5. Conclusions

The current work investigated the liquid water coverage of the interfacial area available for mass transport between the channel and the GDL interface. Three algorithms were developed and implemented as part of this work. One algorithm segmented out the water in the image sequences and found the ratio of liquid water in the channels. Second algorithm looks for the width of the water features. If the water features bridge the entire channel, it is classified as a slug flow; otherwise it is classified as a film. The liquid water coverage in the different channels has also been compared using a third algorithm for channel-to-channel variation in the ACR.

The area coverage ratio was determined for different flow and temperature conditions. It was found that the area coverage ratio decreases at higher current densities. It was also observed that the area coverage ratio decreases with increasing temperatures. This is attributed to the higher saturation temperature leading to less liquid water presence in the channels, and the increased air velocity, which reduces the residence time of the water features within the reactant channels.

The dominant flow pattern for the two-phase flow at the different temperature and flow conditions was also investigated. Higher current densities and higher temperatures, both favored the transition to film flow regime. Slug flow was found to be dominant at the lower current densities at ambient conditions. However, with increased temperature, no slug flow was observed.

Channel-to-channel variation of liquid water coverage was also examined. No defining pattern in the variation of presence of liquid water in the channels was observed. These results are encouraging, as they illustrate that the side channels are not locations for pinning of liquid water, so the channels maintain an unblocked flow of reactants. An unpredictable variation in the channels also shows that the reactant channels are not biased for or against the presence of liquid water. Therefore the results can be extrapolated to flow fields with more or less number of channels without increasing the error in the results.

A comparison was made to neutron radiographs, which highlight the presence of liquid water in the anode and cathode reactant channels. The results show similar trends in the presence of liquid water. This demonstrates the ex-situ investigation reported in this work is also valid under in situ testing conditions.

A correlation has also been proposed which predicts the liquid water area coverage in the reactant channels, based on the operating conditions. The proposed correlation predicts the ACR based on the temperature and gas flow velocity, and has an error less than 20% over the entire range of parameters tested.

Acknowledgments

References

[1] L. Hui, T. Yanghua, W. Zhenwei, S. Zheng, W. Shaohong, S. Datong, Z. Jianlu, K. Fatih, Z. Jiujun, W. Haijiang, L. Zhongsheng, R. Abouatallah, A. Mazza, J. Power Sources 178 (2008) 103.
[2] S. Kandlikar, Mech. Eng. 131 (2009) 4.
[3] S.G. Kandlikar, Heat Transfer Eng. 29 (2008) 575.
[4] W. Dai, H. Wang, X.-Z. Yuan, J.J. Martin, D. Yang, J. Qiao, J. Ma, Int. J. Hydrogen Energy 34 (2009) 9461.
[5] R. Anderson, L. Zhang, Y. Ding, M. Blanco, X. Bi, D.P. Wilkinson, J. Power Sources 195 (2010) 4531.
[6] E. Misran, N.S.M. Hassan, W.R.W. Daud, E.H. Majlan, M.I. Rosli, Int. J. Hydrogen Energy 38 (2013) 9401.
[7] P.K. Jithesh, A.S. Bansode, T. Sundararajan, S.K. Das, Int. J. Hydrogen Energy 37 (2012) 17158.
[8] S. Rakhshanpouri, S. Rowshanzamir, Energy 50 (2013) 220.
[9] E. See, S.G. Kandlikar, ECS Trans. (2012).
[10] M. Grimm, E.J. See, S.G. Kandlikar, Int. J. Hydrogen Energy 37 (2012) 12489.
[11] J.P. Owejan, J.J. Gagliardo, J.M. Sergi, S.G. Kandlikar, T.A. Trabold, Int. J. Hydrogen Energy 34 (2009) 3436.
[12] M. Hossain, S.Z. Islam, A. Colley-Davies, E. Adom, Renew. Energy 50 (2013) 763.
[13] A. Su, F.-B. Weng, C.-Y. Hsu, Y.-M. Chen, Int. J. Hydrogen Energy 31 (2006) 1031.
[14] É. Fontana, E. Mancusi, A.A. Ulson de Souza, S.M.A. Guelli Ulson de Souza, J. Power Sources 234 (2013) 260.
[15] J. Wu, X. Zi Yuan, H. Wang, M. Blanco, J.J. Martin, J. Zhang, Int. J. Hydrogen Energy 33 (2008) 1747.
[16] A. Bazylak, Int. J. Hydrogen Energy 34 (2009) 3845.
[17] K. Tüber, D. Pócza, C. Hebling, J. Power Sources 124 (2003) 403.
[18] M.M. Daino, S.G. Kandlikar, ASME, 2009, pp. 467–479.
[19] D. Spernjak, S.G. Advani, A.K. Prasad, J. Electrochem. Soc. 156 (2009) B109.
[20] F.-B. Weng, A. Su, C.-Y. Hsu, C.-Y. Lee, J. Power Sources 157 (2006) 674.
[21] Z. Zhan, C. Wang, W. Fu, M. Pan, Int. J. Hydrogen Energy 37 (2012) 1094.
[22] R. Satija, D.L. Jacobson, M. Arif, S.A. Werner, J. Power Sources 129 (2004) 238.
[23] P. Boillat, D. Kramer, B.C. Seyfang, G. Frei, E. Lehmann, G.G. Scherer, A. Wokaun, Y. Ichikawa, Y. Tasaki, K. Shinohara, Electrochem. Commun. 10 (2008) 546.
[24] D. Kramer, J. Zhang, R. Shimoi, E. Lehmann, A. Wokaun, K. Shinohara, G.G. Scherer, Electrochim. Acta 50 (2005) 2603.
[25] T.A. Trabold, J.P. Owejan, D.L. Jacobson, M. Arif, P.R. Huffman, Int. J. Heat Mass Transfer 49 (2006) 4712.
[26] I. Manke, C. Hartnig, M. Grünerbel, W. Lehnert, N. Kardjilov, A. Haibel, A. Hilger, J. Banhart, H. Riesemeier, Appl. Phys. Lett. 90 (2007) 174105.
[27] S.-G. Kim, S.-J. Lee, J. Power Sources 230 (2013) 101.
[28] S.-J. Lee, S.-G. Kim, G.-G. Park, C.-S. Kim, Int. J. Hydrogen Energy 35 (2010) 10457.
[29] Z. Dunbar, R.I. Masel, J. Power Sources 171 (2007) 678.
[30] E.J. See, R. Banerjee, M.M. Daino, J.M. Sergi, M. Koz, J.P. Owejan, J.J. Gagliargo, S.G. Kandlikara, (n.d.).
[31] J.M. Sergi, S.G. Kandlikar, Int. J. Hydrogen Energy 36 (2011) 12381.
[32] X. Liu, H. Guo, F. Ye, C.F. Ma, Int. J. Hydrogen Energy 33 (2008) 1040.
[33] I.S. Hussaini, C.-Y. Wang, J. Power Sources 187 (2009) 444.
[34] S. Nirunsin, Y. Khunatorn, J. Sustain. Energy Environ. (2010) 129.
[35] J.M. Sergi, Z. Lu, S.G. Kandlikar, ASME, 2009, pp. 303–311.
[36] O.F. Selamet, U. Pasaogullari, D. Spernjak, D.S. Hussey, D.L. Jacobson, M.D. Mat, Int. J. Hydrogen Energy 38 (2013) 5823.
[37] Z. Lu, S.G. Kandlikar, C. Rath, M. Grimm, W. Domigan, A.D. White, M. Hardbarger, J.P. Owejan, T.A. Trabold, Int. J. Hydrogen Energy 34 (2009) 3445.
[38] Z. Lu, C. Rath, G. Zhang, S.G. Kandlikar, Int. J. Hydrogen Energy 36 (2011) 9864.
[39] H. Yang, T.S. Zhao, P. Cheng, Int. J. Heat Mass Transfer 47 (2004) 5725.
[40] L. Zhang, X.T. Bi, D.P. Wilkinson, R. Anderson, J. Stumper, H. Wang, Chem. Eng. Sci. 66 (2011) 3377.
[41] R. Anderson, D.P. Wilkinson, X. Bi, L. Zhang, J. Power Sources 195 (2010) 4168.
[42] G. Zhang, S.G. Kandlikar, Int. J. Hydrogen Energy 37 (2012) 2412.
[43] S.G. Kandlikar, Z. Lu, Appl. Therm. Eng. 29 (2009) 1276.
[44] S. Yu, D. Jung, Renew. Energy 33 (2008) 2540.
[45] E. Endoh, S. Terazono, H. Widjaja, Y. Takimoto, Electrochem. Solid State Lett. 7 (2004) A209.
[46] C. Spiegel, Designing and Building Fuel Cells, Mcgraw-hill, 2007.
[47] F.P. Incropera, Fundamentals of Heat and Mass Transfer, John Wiley, 2007.
[48] P. Soille, Morphological Image Analysis: Principles and Applications, second ed., Springer, Berlin; New York, 2003.
[49] S.G. Kandlikar, Z. Lu, W.E. Domigan, A.D. White, M.W. Benedict, Int. J. Heat Mass Transfer 52 (2009) 1741.
[50] Z. Lu, M.M. Daino, C. Rath, S.G. Kandlikar, Int. J. Hydrogen Energy 35 (2010) 4222.